Available online at www.sciencedirect.com
ScienceDirect
Journal of Catalysis 249 (2007) 59–66
JOURNAL OF CATALYSIS
www.elsevier.com/locate/jcat

Microstructures and photoactivity of mesoporous anatase hollow microspheres fabricated by fluoride-mediated self-transformation

Jiaguo Yu *, Shengwei Liu, Huogen Yu

State Key Laboratory of Advanced Technology for Material Synthesis and Processing, Wuhan University of Technology, Luoshi Road #122, Wuhan 430070, PR China

Received 17 January 2007; revised 30 March 2007; accepted 30 March 2007

Abstract

Bimodal mesoporous anatase-phase TiO_2 hollow microspheres are one-pot fabricated by hydrothermal treatment of acidic $Ti(SO_4)_2$ solution with NH_4F. Fluoride not only induces the outward hollowing of the spherical TiO_2 aggregates, but also promotes the crystallization of primary anatase TiO_2 nanocrystals, resulting in enlarged crystallite sizes and decreased specific surface areas. The hierarchical mesopores exhibit peak intra-aggregated mesopore sizes of 3–10 nm and peak interaggregated mesopore sizes of 30–50 nm, depending on the specific molar ratio of fluoride to titanium ($\boldsymbol{R}$). The pore volume increases in parallel with the average pore size with increasing $\boldsymbol{R}$ until the collapse of interaggregated pores at $\boldsymbol{R} = 2$. The photocatalytic efficiency in decomposition of gaseous acetone by as-obtained hollow TiO_2 microspheres generally exceeds that by Degussa P25 when $\boldsymbol{R}$ is <2. The influence of fluoride on photoactivity are discussed in terms of phase structures and pore structures.
© 2007 Elsevier Inc. All rights reserved.

Keywords: Hollow; Titania; Microspheres; Hydrothermal synthesis; Fluoride; Microstructure; Photocatalytic activity

1. Introduction

Since Honda and Fujishima discovered the photocatalytic splitting of water on TiO_2 electrodes in 1972 [1–6], considerable effort has been devoted to developing highly active oxide semiconductor photocatalysts for their wide application in solar energy conversion and environmental protection. Among the various oxide semiconductor photocatalysts, titania has proven the most suitable for widespread environmental applications due to its biological and chemical inertness, strong oxidizing power, cost-effectiveness, and long-term stability against photocorrosion and chemical corrosion [3]. The strong oxidizing power of TiO_2 photocatalyst has been ascribed to highly oxidative valence band holes (+2.7 V vs the normal hydrogen electrode at pH 7) and various oxygen-containing radical species (e.g., $\cdot OH$, O_2^-, $HO_2\cdot$) generated on the UV-illuminated TiO_2 surface [2]. However, the performance of TiO_2 requires further enhancement from the standpoint of widely practical applications and commercial benefits, due in part to its narrow light-response range as well as its low quantum efficiency [2,3,5,6]. Consequently, numerous works focused on enhancing the photocatalytic performance of TiO_2 by doping, metal deposition, surface sensitization, coupling of composite semiconductors, and other methods [2,4]. In particular, it has been demonstrated that the photocatalytic activity of titania is strongly dependent on its phase structure, crystallite size, specific surface areas, and pore structure [7,8].

Although TiO_2 of varying morphologies and textures has been synthesized and investigated in previous studies, the fabrication of TiO_2 hollow structures merits special attention due to these structures' low density, high surface area, good surface permeability, and greater light-harvesting capacity. Moreover, higher energy conversion efficiency and photocatalytic activity are expected using TiO_2 hollow structures as photocatalysts [9–13]. Up to now, most of the approaches for hollow structures rely on the use of sacrificial templates (either hard or soft), with the desired hollow interiors generated on the removal of templates by calcination or dissolu-

* Corresponding author.
E-mail address: jiaguoyu@yahoo.com (J. Yu).

0021-9517/$ – see front matter © 2007 Elsevier Inc. All rights reserved.
doi:10.1016/j.jcat.2007.03.032

Table 1
Effect of experimental parameters on the physical properties of TiO_2 samples

No.	R[a]	T and t[b]	Crystallite size[c] (nm)	Crystallinity[d]	S_{BET}[e] ($m^2\ g^{-1}$)	Pore volume[f] ($cm^3\ g^{-1}$)	Average pore size[g] (nm)
TSF-001	0	180 °C 3 h	10	1	170	0.15	3.6
TSF-002	0	180 °C 9 h	11	1.1	124	0.17	5.6
TSF-003	0	200 °C 9 h	15	1.5	96	0.18	7.3
TSF-004	0.4	180 °C 3 h	16	1.4	94	0.19	8.0
TSF-005	0.4	180 °C 9 h	23	1.8	83	0.19	9.3
TSF-006	0.4	200 °C 9 h	23	1.9	69	0.21	12.2
TSF-007	1	180 °C 3 h	25	1.9	67	0.22	13.2
TSF-008	1	180 °C 9 h	34	2.4	68	0.22	13.2
TSF-009	1	200 °C 9 h	35	2.5	51	0.22	16.9
TSF-010	1	200 °C 36 h	38	2.6	52	0.17	12.7
TSF-011	2	180 °C 3 h	41	2.5	40	0.10	9.7
TSF-012	2	180 °C 9 h	51	3.0	31	0.09	11.0
TSF-013	2	200 °C 9 h	57	3.4	22	0.07	12.6
TSF-014	2	200 °C 36 h	72	3.8	21	0.07	12.9

[a] R denotes the molar ratio of fluoride to titanium.
[b] T & t denote the hydrothermal temperature and time, respectively.
[c] Average crystalline size is determined by the broadening of anatase (101) plane diffraction peak using Scherrer equation.
[d] The relative crystallinity is evaluated via the relative intensity of anatase (101) plane diffraction peak using the sample obtained by hydrothermal treatment without fluoride at 180 °C for 3 h as reference.
[e] The BET surface area is determined by a multipoint BET method using the adsorption data in the relative pressure (P/P_0) range from 0.05 to 0.3.
[f] Pore volume is determined by adsorption branch of the N_2 isotherms at $P/P_0 = 0.994$.
[g] Average pore size is estimated using the adsorption branch of the N_2 isotherms using BJH method.

tion [9,10]. To overcome the complexity associated with the templating method, one-pot template-free methods for hollow structures have been developed based on direct solid evacuation with Ostwald ripening and the Kirkendall effect, as well as self-assembly of preformed building blocks through oriented attachment [11,14–16]. Large-scale production of well-crystallized hollow anatase-phase TiO_2 microspheres with high photocatalytic activity remains a great challenge, however [12,13,17].

It has been suggested that surface fluorination of TiO_2 can enhance the photocatalytic decomposition of phenol in aqueous solution, which is ascribed to an increased number of hydroxyl radicals on the surface of fluorinated TiO_2 [18–20]. We have shown that photocatalytic decomposition of gas-phase acetone can be greatly enhanced by F-doped TiO_2 due to a reduced electron–hole recombination rate [21]. In addition, it also has been demonstrated that F-doping in TiO_2 can induce visible-light-driven photocatalytic activity by creating oxygen vacancies [22,23]. However, most of these previous studies concentrated on the modification effect of fluoride on either the surface structure or the electronic structure of as-prepared TiO_2 products; the effect of fluoride on the textural microstructure of TiO_2 samples has been considered less often [24]. In the present work, we fabricated anatase-phase TiO_2 hollow microspheres in large scale by a fluoride-mediated hydrothermal process based on our recently discovered approach [16]. We carefully investigated the effects of fluoride on the microstructures, especially on the pore structures of as-prepared hollow microspheres, and evaluated the photocatalytic decomposition of acetone in air.

2. Experimental

2.1. Sample preparation

The hollow TiO_2 microspheres were prepared as reported previously [16]. First, dilute H_2SO_4 solution (1 M) was prepared from concentrated H_2SO_4 and distilled water. Then $Ti(SO_4)_2$ was dissolved in this solution to give a $Ti(SO_4)_2$ concentration of 0.5 M. This solution was clear and stable for several days at room temperature. The as-prepared acidic $Ti(SO_4)_2$ solution was mixed with 50 mL of NH_4F solution under vigorous stirring. The molar ratio of fluoride to titanium (R) varied from 0 to 2 (0, 0.4, 1, and 2). The solution was transferred to a 100-mL Teflon-lined autoclave, which was then filled with water up to 80% of the total volume. The autoclave was sealed and kept at 200 °C for about 9 h. The white precipitate was collected, washed with distilled water several times, and then dried at 80 °C for 6 h. A serial of experiments with varying hydrothermal temperature and time were also carried out for comparison, as presented in Table 1.

2.2. Characterization

X-ray powder diffraction (XRD) patterns were obtained on a D/Max-RB X-ray diffractometer (Rigaku, Japan) using Cu$K\alpha$ radiation at a scan rate of 0.05° 2θ s^{-1}. Scanning electron microscopy (SEM) was carried out using a JEM-6330F microscope (JEOL, Japan) at an accelerating voltage of 10 kV, linked with an Oxford Instruments X-ray analysis system. Samples for SEM were air-dried and platinum-coated with

an Edwards S150B sputter-coater. Transmission electron microscopy (TEM) analysis and selected area electron diffraction (SAED) were conducted using a JEOL 1200 EX at 120 kV. The Brunauer–Emmett–Teller (BET) surface area of the powders was analyzed by nitrogen adsorption in a Micromeritics ASAP 2020 nitrogen adsorption apparatus. All of the samples were degassed at 180 °C before nitrogen adsorption measurements. The BET surface area was determined by a multipoint BET method using the adsorption data in the relative pressure (P/P_0) range of 0.05–0.3. A desorption isotherm was used to determine the pore size distribution by the Barret–Joyner–Halender (BJH) method, assuming a cylindrical pore modal [25,26]. The nitrogen adsorption volume at the relative pressure (P/P_0) of 0.994 was used to determine the pore volume and average pore size.

2.3. Measurement of photocatalytic activity

Acetone, formaldehyde, and other volatile organic compounds (VOCs) are common indoor air pollutants in modern houses that have been the subject of numerous complaints regarding health disorders, such as leukemia, nausea, headache, and fatigue. These harmful gases usually come from the plywood, particleboard, and adhesives used for wall coverings used in construction and furnishing. To improve indoor air quality, these VOCs must be eliminated. Consequently, we chose acetone as a model contaminate chemical. Photocatalytic oxidation of acetone is based on the following reaction [21,27]:

$$CH_3COCH_3 + 4O_2 \rightarrow 3CO_2 + 3H_2O. \quad (1)$$

The photocatalytic activity experiments on the as-prepared TiO_2 samples were performed according to procedures reported previously [8,21]. The weight of the photocatalyst used for each experiment was kept at about 0.3 g. The analysis of acetone, carbon dioxide, and water vapor concentration was conducted online with a Photoacoustic IR Multigas Monitor (INNOVA Air Tech Instruments Model 1312) [8,21]. The acetone vapor was allowed to reach adsorption equilibrium with the catalyst in the reactor before UV light irradiation. The initial concentration of acetone after the adsorption equilibrium, about 275 ± 25 ppm, remained constant for about 10 min. The initial concentration of water vapor was 1.20 ± 0.01 vol%, and the initial temperature was 25 ± 1 °C. A 15-W, 365-nm UV lamp (4 cm above the dishes) (Cole-Parmer Instruments) was used as the light source to trigger the photocatalytic reaction. Each set of experiments was followed for 60 min. The photocatalytic activity of the powders was quantitatively evaluated by comparing the apparent rate constants (k_a). The photocatalytic degradation of acetone has been proved to follow a Langmuir–Hinshelwood mechanism [3,4,8,21], and the k_a is deduced to approximately conform to the following equation [8,21]:

$$\ln \frac{c_0}{c_t} = k_a t, \quad (2)$$

where c_0 and c_t represent the initial equilibrium concentration of the acetone and the reaction concentration of acetone, respectively.

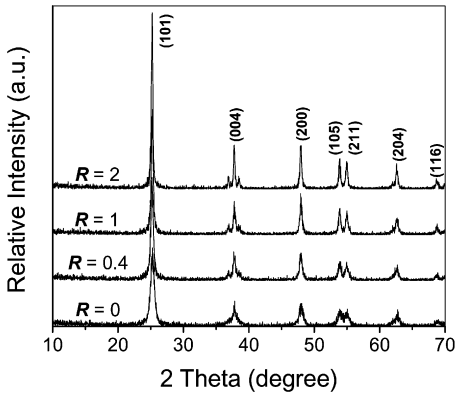

Fig. 1. XRD patterns of TiO_2 samples prepared with varying $\boldsymbol{R}$ at 200 °C for 9 h.

The photocatalytic activity of P25 was also measured as a reference to compare with that of the synthesized catalysts. Each set of photocatalytic measurements was repeated three times, and the experimental error was found to be within ±5%.

3. Results and discussion

3.1. Phase structure

The phase structure, crystallite size, and crystallinity of TiO_2 have been demonstrated to be of great importance for its photocatalytic activity; for example, many studies have confirmed that anatase phase of titania shows higher photocatalytic activity than brookite or rutile phase [2]. XRD was used to investigate the changes of phase structure of TiO_2 samples prepared in varying molar ratio of fluoride to titanium ($\boldsymbol{R}$). Fig. 1 shows XRD patterns of the TiO_2 samples prepared with varying $\boldsymbol{R}$ at 200 °C for 9 h. All of the as-prepared samples appeared to be phase-pure anatase [JCPDS no. 21-1272, space group: $I4_1/amd$ (141)]. Usually, the phase transformation temperature from amorphous to anatase of TiO_2 is above 400 °C. Thus, it can be concluded that the phase transformation from amorphous to anatase is favored and promoted in the present reaction system.

This property may be ascribed to the cooperative effect of at least three factors. First, a nonequilibrium pressure environment in hydrothermal treatment promotes the low-temperature phase transformation from amorphous to anatase [28]. Second, the existence of water in the hydrothermal treatment catalyzes the change of localized structure of amorphous titania to anatase structure, resulting in acceleration of anatase nucleation [29,30]. In addition, the presence of F^- and SO_4^{2-} in the present acid reaction condition also should play an important role in promoting the phase transformation. It is well known that the phase transformation of TiO_2 occurs due to the rearrangement of TiO_6 octahedra. The crystallization process of anatase phase from amorphous TiO_2 was postulated to initiate through face-sharing polycondensation of these octahedra [30,31]. According to the surface acidic and basic properties described by Bahnemann et al. [30–32] and the isoelectric point of TiO_2 (pH 5.5–6) [33,34], the surface Ti–OH groups in TiO_6 octahedra should be at least partially protonated to give $TiOH_2^+$ in

an acidic environment (pH ca. 1). Therefore, TiO_2 formed under acidic conditions will have a positive surface charge density and will be expected to experience significant electrostatic attraction with negatively charged anions. Consequently, both SO_4^{2-} and F^- will interact with TiO_6 octahedra by surface absorption in addition to coordination. Of course, F^- also might interact with TiO_6 octahedra by hydrogen bonding. Although more work is needed to clearly illustrate these rather complex interactions, it is believed that the interaction of these anionic species with the TiO_6 octahedra should favor the formation of anatase phase due to specific spatial effects beneficial to the face-sharing polycondensation between TiO_6 octahedra [12,35].

Further observation shows that with increasing $\boldsymbol{R}$, XRD peak intensities of anatase become steadily stronger and the width of XRD diffraction peaks of anatase becomes slightly narrower, indicating the enhancement of crystallization and formation of greater TiO_2 crystallites. This is further confirmed by the quantitatively evaluated results shown in Table 1. The relative crystallinity was estimated based on the relative intensity of the (101) diffraction peak [28]. The average crystallite size was estimated based on the broadening of (101) diffraction peak using Scherrer's equation [36]. The result is in good agreement with a previous report that F^- enhanced the crystallization of anatase phase and promoted crystallite growth [21,24,37]. We can explain this result based on at least two factors, as follows. First, nucleophilic substitution is favored due to the higher electronegativity of F^- (compared with SO_4^{2-}), which in turn reduces the chemical reactivity of the precursor [38]. The nucleation of anatase is thus suppressed, and fewer critical nuclei are formed. As a result, sufficient nutrients are left to allow greater anatase crystallite growth during the subsequent hydrothermal treatment. Second, it has been proved that crystallite growth involves a dissolution–recrystallization mechanism during hydrothermal treatment [16,29,30,39]. In the present case, the added fluoride will be helpful for dissolution of the amorphous counterparts, taking into account the etching effect of F^- in the acidic condition (pH ca. 1). Moreover, the hydrogen-bonding and surface absorption of F^- to the protonated TiO_6 octahedra should enhance the mobility of these octahedra due to lower electrostatic repulsion inhibition during transport. As discussed in more detail below, in the formation of as-prepared hollow TiO_2, the added fluoride helps both the dissolution of the interior and the subsequent mass transfer from the interior to the surface, providing abundant nutrients for the crystallite growth of preformed nuclei on the surface.

A similar trend toward changes in phase structure, crystallite size, and crystallinity was also observed for the products obtained in varying $\boldsymbol{R}$ at 180 °C for 9 h (as shown in Table 1). In addition, increasing temperature and/or time favor greater crystallites and enhanced crystallinity, which is consistent with our previous reports [28].

3.2. Morphological aspects

TiO_2 hollow microspheres are prepared by hydrothermal treatment of the $Ti(SO_4)_2$ and NH_4F mixture. Samples prepared with varying $\boldsymbol{R}$ at 200 °C for 9 h were investigated by SEM and TEM. In the absence of fluoride, the products were solid microspheres with a diameter of about 1 μm (Fig. 2a). The hollow structures were readily formed as NH_4F was added into the reaction system. At $\boldsymbol{R} = 0.4$, hollow microspheres could be clearly observed, but a fraction of solid TiO_2 microspheres still existed (Fig. 2b). When $\boldsymbol{R}$ increased to certain degree ($\boldsymbol{R} = 1$), most of the microspheres appeared to have hollow interiors, as shown in Fig. 2c. SEM images (Fig. 2d) further confirmed the presence of hollow structures and indicated that the rough external shells of the hollow microspheres consisted of loosely packed nanoparticles. As $\boldsymbol{R}$ increased further, the shells of the hollow microspheres were progressively thinned (Fig. 2e). Therefore, it can be deduced that the hollowing process of solid microspheres was mediated by fluoride; the hollowing rate was related to $\boldsymbol{R}$, with higher $\boldsymbol{R}$ resulting in a greater hollowing rate. The fluoride may have been helpful for dissolution of the interior and mass transfer from the interior to the external surface.

A typical SAED analysis (inset in Fig. 2c) indicated that the shell wall consisted of a polycrystalline aggregate of anatase nanoparticles [d-spacings and $\{hkl\}$ values: 0.351 (101), 0.238 (004), 0.189 (200), 0.169 (105), and 0.166 nm (211); space group: $I4_1/amd$ (141); $a = 3.785$ Å, $c = 9.514$ Å; JCPDS no. 21-1272]. This is consistent with XRD studies shown in Fig. 1. The energy-dispersive X-ray (EDX) analysis spectrum (Fig. 3) detected no N, F, or S elementals, as expected, with the peaks at 4.5, 4.9, and 0.45 keV corresponding to Ti. A peak for oxygen at 0.52 keV was observed, with a Ti/O atomic ratio of 1:2. These findings are in good agreement with previous reports [12,16].

The formation process of as-prepared hollow TiO_2 microspheres was investigated by the time-dependent evolution experiment. Fig. 4 shows the TEM images of samples obtained with $\boldsymbol{R} = 1$ at 200 °C for varying hydrothermal times. The samples collected at 30 min were solid spheres (Fig. 4a), which turned out to be amorphous (XRD result; inset in Fig. 4a). When the hydrothermal time was prolonged to 9 h, the samples appeared as hollow microspheres (Fig. 4b). The shells were increasingly thinned with further prolonged hydrothermal time (Fig. 4c). Notably, the average particle size increased slightly during the formation of hollow microspheres. The average particle size increased with increasing hydrothermal time, from 0.9 μm at 30 min to 1 μm at 9 h, and eventually to 1.2 μm at 36 h. Based on these findings, the formation of hollow TiO_2 microspheres can be understood in terms of fluoride-mediated self-transformation from amorphous solid TiO_2 precursors by localized Ostwald ripening, in which preferential dissolution of the particle interior is coupled with the deposition of loosely packed nanocrystals on the surfaces of external shells [16].

In addition, it is noteworthy that a significant fraction of titania particles tends to fuse together in form of dimers, trimers, and tetramers, somewhat similar to findings in previous studies [40]. The dimerization process should be induced by titania condensation as two separate titania microspheres consisting of Ti–OH group on the surface contact each other.

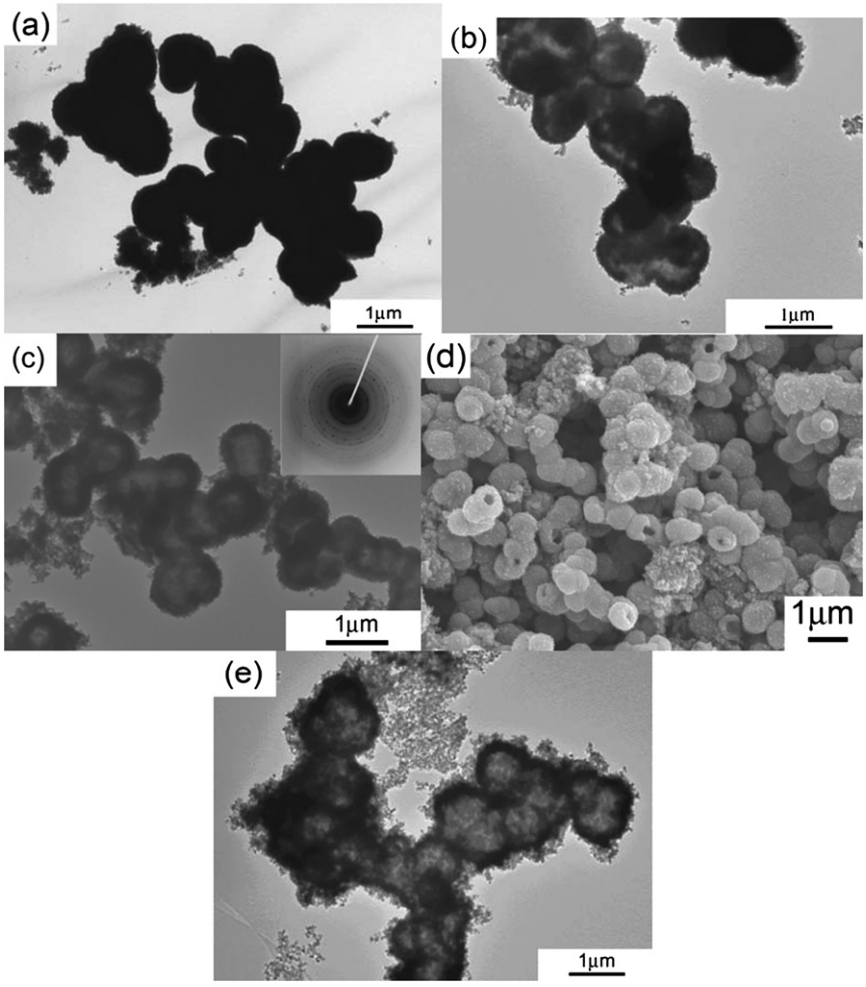

Fig. 2. TEM (a, b, c, e) and SEM (d) images of TiO_2 samples prepared with varying $\boldsymbol{R}$ at 200 °C for 9 h: (a) 0; (b) 0.4; (c, d) 1; (e) 2. Inset in (c) shows the corresponding SAED pattern.

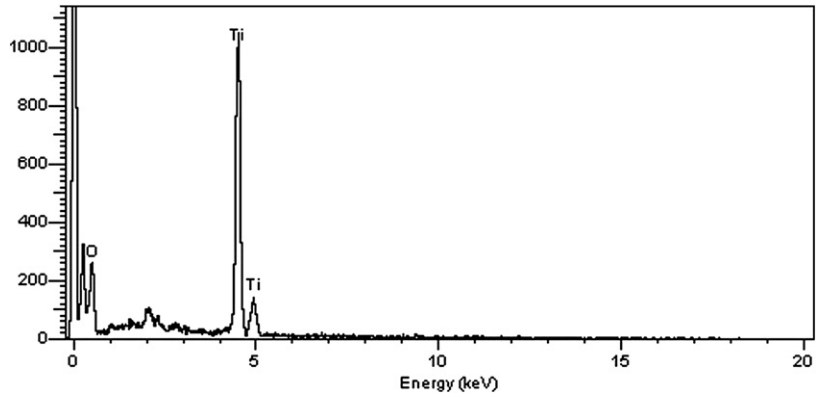

Fig. 3. EDX spectrum of anatase TiO_2 hollow microspheres obtained with $\boldsymbol{R} = 1$ at 200 °C for 9 h.

3.3. Pore structure and BET surface areas

It is widely accepted that gas–solid heterogeneous photocatalysis is a surface-based process, and thus a large surface area has positive effects on such a process [2–4]. A larger surface area provides more surface active sites for the adsorption of reactants molecules, making the photocatalytic process more efficient [7,28]. Moreover, the porous structure is believed to facilitate the transportation of reactant molecules and products through the interior space due to the interconnected porous networks and to favor the harvesting of exciting light due to enlarged surface area and multiple scattering within the porous framework [8,41]. Consequently, we carefully investigated the effects of fluoride on the pore structure and BET surface areas of as-prepared TiO_2 samples based on nitrogen adsorption and desorption measurements.

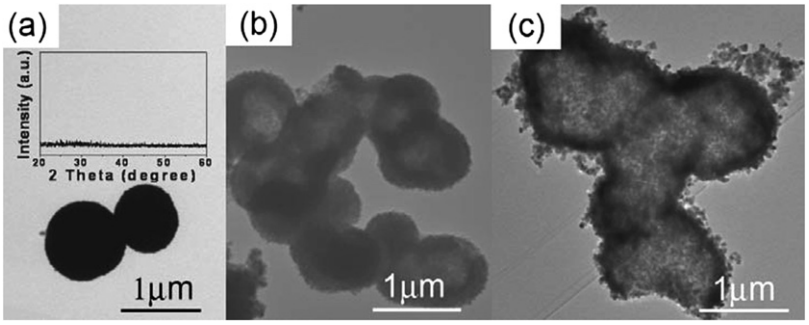

Fig. 4. TEM images of TiO_2 samples prepared with $\boldsymbol{R} = 1$ at 200 °C for varying hydrothermal time: (a) 30 min; (b) 9 h; (c) 36 h. Inset in (a) shows the corresponding XRD pattern.

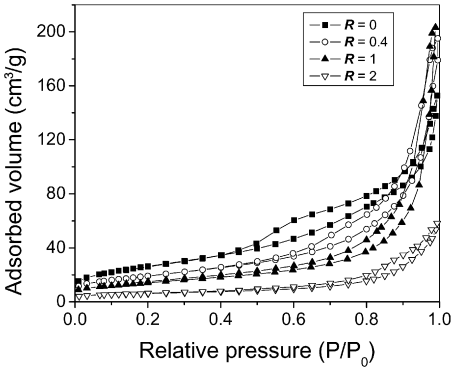

Fig. 5. Nitrogen adsorption–desorption isotherms of the TiO_2 samples prepared with varying $\boldsymbol{R}$ at 200 °C for 9 h.

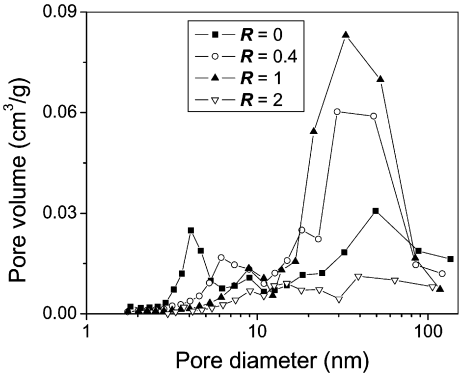

Fig. 6. Pore size distribution curves of the TiO_2 samples prepared with varying $\boldsymbol{R}$ at 200 °C for 9 h.

Fig. 5 shows the nitrogen adsorption and desorption isotherms of TiO_2 samples obtained at 200 °C for 9 h with varying $\boldsymbol{R}$. The isotherm corresponding to the sample obtained without fluoride is of type IV (BDDT classification) with two capillary condensation steps, implying bimodal pore size distributions in the mesoporous and macroporous regions. According to previous reports [8,28,42], a bimodal mesopore size distribution results from two different aggregates in the powders. The hysteresis loop in the lower relative pressure range ($0.4 < P/P_0 < 0.8$) is related to finer intra-aggregated pores formed between intra-agglomerated primary particles, and that in the higher relative pressure range ($0.8 < P/P_0 < 1$) is associated with larger interaggregated pores produced by interaggregated secondary particles. This bimodal mesopore size distribution is further confirmed by the corresponding pore size distributions shown in Fig. 6. The powder contained small mesopores (ca. 3 nm) and larger mesopores with a maximum pore diameter of ca. 48 nm. The presence of fluoride in the synthetic system exerted significant influence on the pore structure and BET surface areas of the obtained products. With increasing $\boldsymbol{R}$, the shapes of nitrogen adsorption and desorption isotherms underwent several obvious changes, implying a significant variation of pore structures. First, the isotherms corresponding to the samples obtained at $\boldsymbol{R} = 0.4$ and 1 (compared with that at $\boldsymbol{R} = 0$) show higher absorption at high relative pressures (P/P_0 approaching 1), indicating the formation of macropores and/or an increasing pore volume. This may be related to the fluoride-mediated hollowing of the interior space of TiO_2 microspheres (as shown in Figs. 2b and 2c). Second, with increasing $\boldsymbol{R}$, the two separate hysteresis loops gradually joined together as one loop, implying that the pore size distributions of intra-aggregated and interaggregated pores tend to overlap, as confirmed in Fig. 6. This affect is associated with growth of the crystallites and shrinkage of the aggregates, resulting in a right shift of intra-aggregated pores and a left shift of interaggregated pores. In addition, it is interesting to note that with increasing $\boldsymbol{R}$ from 0 to 1, the hysteresis loops shifted to a higher relative pressure (P/P_0) region; the relative areas of the hysteresis loops in higher relative pressure range increased gradually and eventually dominated the total areas of the entire hysteresis loops. These results suggest that the pore volume of interaggregated pores increased and gradually became the main portion of the total pore volume. As further confirmed in Fig. 6, the pore volumes of intra-aggregated mesopores were negligible compared with those of the interaggregated ones, based on their corresponding integral areas. However, when $\boldsymbol{R}$ was further increased to 2, the area of the hysteresis loop decreased significantly, implying the collapse of interaggregated pores, as confirmed by a drastic decrease in the corresponding pore volume (Fig. 6).

Fig. 7 quantitatively shows the changing trends in BET surface area, pore volume, and average pore size with increasing $\boldsymbol{R}$. Each sample shows a monotonic decrease in the BET surface area with increasing $\boldsymbol{R}$ due to the crystallite growth. In most cases, the pore volume decreased with increasing average pore size [28]; however, the pore volume of as-prepared

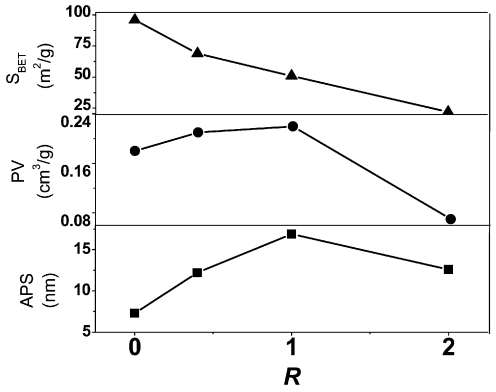

Fig. 7. BET surface area, pore volume and average pore size of TiO_2 samples prepared at 200 °C for 9 h as a function of $\boldsymbol{R}$. S_{BET}, PV and APS denote BET surface area, pore volume and average pore size, respectively.

TiO_2 samples increased in parallel with average pore size with increasing $\boldsymbol{R}$. Why did this occur? The total pore volume evaluated by the nitrogen adsorption and desorption measurement is mainly the sum of pore volume of micropores and mesopores [25,26]. As noted earlier, the total pore volume of an as-prepared TiO_2 sample is determined mainly by that of the interaggregated mesopores, which in turn are promoted with increasing $\boldsymbol{R}$ until they are collapsed as $\boldsymbol{R}$ increases to 2. Therefore, both the pore volume and average pore size increased gradually with increasing $\boldsymbol{R}$ up to 2, at which point the pore volume as well as the average pore size suddenly decreased.

The effects of hydrothermal temperature and/or time on the pore structure and BET surface areas of TiO_2 products were also found to be highly dependent on $\boldsymbol{R}$, as shown in Table 1. On one hand, with increasing hydrothermal temperature (or time), the pore volume increased at lower $\boldsymbol{R}$ (0 and 0.4) but decreased at higher $\boldsymbol{R}$ (1 and 2); this increase may be ascribed to increasing pore volume of interaggregated pores, whereas the decrease can be assigned to the collapse of interaggregated pores. On the other hand, with increasing hydrothermal time, the BET surface area decreased at both lower $\boldsymbol{R}$ (0 and 0.4) and higher $\boldsymbol{R}$ (2), but increased slightly at moderate $\boldsymbol{R}$ (1). The crystallite size increased with increasing hydrothermal time (Table 1), and the BET surface area should decrease. We speculate that the slight increase in BET surface area at moderate $\boldsymbol{R}$ (1) is associated with the hollowing of the interiors of TiO_2 microspheres. At moderate $\boldsymbol{R}$, the hollowing rate was moderate; the tiny hollowing interiors were relatively dispersed (Fig. 2), and thus their contribution to the BET surface area was significant.

3.4. Photocatalytic activity

Table 2 shows the dependence of the k_a (10^{-3}, min^{-1}) value of the TiO_2 samples obtained at 200 °C on $\boldsymbol{R}$. The k_a value of the samples obtained without fluoride was 6.96. This good photocatalytic activity is associated with the formation of anatase phase with high crystallinity, bimodal mesopore size distribution, and relatively large BET surface areas. Fluoride had an obvious influence on the photocatalytic activity of the TiO_2 samples. With increasing $\boldsymbol{R}$, the k_a value first increased. The k_a value of the as-obtained sample reached its highest value of 8.77 at $\boldsymbol{R} = 0.4$. This superior photoactivity can be ascribed to the enhanced crystallization and enlarged pore volume (as shown in Table 1). However, when $\boldsymbol{R}$ was further increased to 1 and 2, the k_a value began to drop, likely because the negative effect of fluoride on the photocatalytic activity exceeded its positive effect; that is, the decreased BET surface areas results in a significant decrease in the photocatalytic activity of the samples that cannot be compensated for by the enhanced crystallization and enlarged pore volume. Table 2 also presents the photocatalytic activity of Degussa P25 for comparison. As $\boldsymbol{R}$ increased to 2, the photocatalytic activity of the samples was even slightly lower than that of P25. This may be related to the drastic decrease of pore volume due to the collapse of interaggregated mesopores in addition to smaller BET surface areas. In addition, the sample no longer exhibited a bimodal mesopore size distribution, which should be beneficial to light harvesting and mass transport [7,8]. Specifically, the sample obtained with $\boldsymbol{R} = 0.4$ at 200 °C for 9 h showed the greatest photocatalytic activity, twice that of P25.

Table 2
The apparent rate constant (k_a) of TiO_2 samples prepared at 200 °C for 9 h with varying $\boldsymbol{R}$, and their comparison with that of P25

Samples	$\boldsymbol{R} = 0$	$\boldsymbol{R} = 0.4$	$\boldsymbol{R} = 1$	$\boldsymbol{R} = 2$	P25
k_a (10^{-3}, min^{-1})	6.96	8.77	7.17	3.94	4.07

Based on the preceding discussion, it can be concluded that the photocatalytic activity of as-prepared TiO_2 samples depends on the cooperative effect of crystallinity, BET surface areas, pore volume, and pore size distribution. In particular, the positive effect of fluoride on photocatalytic activity may be ascribed mainly to its effects on pore volume and crystallinity. Of course, the surface structure as well as the electronic structure of TiO_2 product modified by fluoride also should play important roles in enhancing photoactivity, as demonstrated in previous studies [18–23].

Even though hollow structures are generally expected to have larger specific surface areas, our results were usually beyond our expectations. Specific surface area is related to the crystallinity of the particles, with better crystallinity usually resulting in larger crystallites and thus smaller specific surface area. Most hollow TiO_2 structures reported previously exhibited either poor crystallization or smaller BET surface area, and thus low photocatalytic activity. In the present study, we have demonstrated that highly crystallized anatase hollow microspheres with retention of relative high BET surface area can be fabricated using $Ti(SO_4)_2$ as precursor and NH_4F as a crystal modifier by hydrothermal treatment. More importantly, we have shown for the first time that pore volume—another positive factor in enhancing the photoactivity of TiO_2 hollow microspheres—is able to increase simultaneously with the enhanced crystallization in the present synthetic system by adding appropriate amounts of fluoride. This investigation may provide new insight into developing highly photoactive hollow TiO_2 photocatalysts.

4. Conclusion

Hollow anatase-phase TiO_2 microspheres with mesoporous shells can be easily fabricated on a large scale by fluoride-mediated hydrothermal treatment of $Ti(SO_4)_2$ solution. Fluoride induces the hollowing process of TiO_2 microspheres, and the rate of such a process can be readily tuned by changing $\boldsymbol{R}$; a higher $\boldsymbol{R}$ results in a greater hollowing rate. Moreover, the added fluoride promotes the crystallization and crystallite growth of anatase-phase TiO_2 primary nanocrystals, and thus the BET surface areas decrease with increasing $\boldsymbol{R}$. The as-prepared hollow TiO_2 microspheres generally exhibit bimodal mesopore size distribution, finer intra-aggregated pores, and greater interaggregated pores, with maximum pore diameters in the range of 3–10 and 30–50 nm, respectively. The pore volume increases in parallel with average pore size until the collapse of interaggregated mesopores occurs. The positive effect of fluoride on enhanced crystallization and increased pore volume at appropriate $\boldsymbol{R}$ is suggested to be the main contribution of fluoride to improving the photocatalytic activity of hollow TiO_2 microspheres.

Acknowledgments

This work was partially supported by the National Natural Science Foundation of China (grants 20473059 and 50625208) and the Chinese Ministry of Education's Key Research Project (grant 106114) and Program for Changjiang Scholars and Innovative Research Team in University (PCSIRT; grant IRT0547).

References

[1] K. Honda, A. Fujishima, Nature 238 (1972) 37.
[2] O. Carp, C.L. Huisman, A. Reller, Prog. Solid State Chem. 32 (2004) 33.
[3] M.R. Hoffmann, S.T. Martin, W. Choi, D.W. Bahnemann, Chem. Rev. 95 (1995) 69.
[4] A.L. Linsebigler, G. Lu, J.T. Yates, Chem. Rev. 95 (1995) 735.
[5] R. Asahi, T. Morikawa, T. Ohwaki, K. Aoki, Y. Taga, Science 293 (2001) 269.
[6] J. Yu, X. Zhao, Q. Zhao, Thin Solid Films 379 (2000) 7.
[7] F.B. Li, X.Z. Li, M.F. Hou, K.W. Cheah, W.C.H. Choy, Appl. Catal. A 285 (2005) 181.
[8] J. Yu, J.C. Yu, M.K.P. Leung, W. Ho, B. Cheng, X. Zhao, J. Zhao, J. Catal. 217 (2003) 69.
[9] F. Caruso, R.A. Caruso, H. Mohwald, Science 282 (1998) 1111.
[10] A. Imhof, Langmuir 17 (2001) 3579.
[11] T. Nakashima, N. Kimizuka, J. Am. Chem. Soc. 125 (2003) 6386.
[12] H.G. Yang, H.C. Zeng, J. Phys. Chem. B 108 (2004) 3492.
[13] X.X. Li, Y.J. Xiong, Z.Q. Li, Y. Xie, Inorg. Chem. 45 (2006) 3493.
[14] Y.D. Yin, R.M. Rioux, C.K. Erdonmez, S. Hughes, G.A. Somorjai, A.P. Alivisatos, Science 304 (2004) 711.
[15] H.G. Yang, H.C. Zeng, Angew. Chem. Int. Ed. 43 (2004) 5930.
[16] J. Yu, H. Guo, S.A. Davis, S. Mann, Adv. Funct. Mater. 16 (2006) 2035.
[17] D.Y. Zhang, D. Yang, H.J. Zhang, C.H. Lu, L.M. Qi, Chem. Mater. 18 (2006) 3477.
[18] H. Park, W.Y. Choi, J. Phys. Chem. B 108 (2004) 4086.
[19] C. Minero, G. Mariella, V. Maurino, E. Pelizzetti, Langmuir 16 (2000) 2632.
[20] C. Minero, G. Mariella, V. Maurino, D. Vione, E. Pelizzetti, Langmuir 16 (2000) 8964.
[21] J.C. Yu, J. Yu, W. Ho, Z. Jiang, L. Zhang, Chem. Mater. 14 (2002) 3808.
[22] W.K. Ho, J.C. Yu, S.C. Lee, Chem. Commun. (2006) 1115.
[23] D. Li, H. Haneda, N.K. Labhsetwar, S. Hishita, N. Ohashi, Chem. Phys. Lett. 401 (2005) 579.
[24] J. Yu, J.C. Yu, B. Cheng, S.K. Hark, K. Iu, J. Solid State Chem. 174 (2003) 372.
[25] K.S.W. Sing, D.H. Everett, R.A.W. Haul, L. Moscou, R.A. Pierotti, J. Rouquerol, T. Siemieniewska, Pure Appl. Chem. 57 (1985) 603.
[26] S.J. Gregg, K.S.W. Sing, Adsorption, Surface Area and Porosity, Academic Press, London, 1982.
[27] M.E. Zorn, D.T. Tompkins, W.A. Zeltner, M.A. Anderson, Appl. Catal. B 23 (1999) 1.
[28] J. Yu, G. Wang, B. Cheng, M. Zhou, Appl. Catal. B 69 (2007) 171.
[29] K. Yanagisawa, Y. Yamamoto, Q. Feng, N. Yamasaki, J. Mater. Res. 13 (1998) 825.
[30] K. Yanagisawa, J. Ovenstone, J. Phys. Chem. B 103 (1999) 7781.
[31] H.B. Yin, Y. Wada, T. Kitamura, S. Kambe, S. Murasawa, H. Mori, T. Sakata, S. Yanagida, J. Mater. Chem. 11 (2001) 1694.
[32] D. Bahnemann, A. Henglein, L. Spanhel, Faraday Discuss. Chem. Soc. 78 (1984) 151.
[33] N. Kallay, S. Zalac, G. Stefanic, Langmuir 9 (1993) 3457.
[34] R. Rodriguez, M.A. Blesa, A.E. Regazzoni, J. Colloid Interface Sci. 177 (1996) 122.
[35] M.C. Yan, F. Chen, J.L. Zhang, M. Anpo, J. Phys. Chem. B 109 (2005) 8673.
[36] J.C. Yu, J. Yu, W. Ho, L. Zhang, Chem. Commun. (2001) 1942.
[37] J. Yu, H. Yu, B. Cheng, X. Zhao, J.C. Yu, W. Ho, J. Phys. Chem. B 107 (2003) 13871.
[38] S. Yamabi, H. Imai, Chem. Mater. 14 (2002) 609.
[39] J. Yu, J.C. Yu, W. Ho, L. Wu, X. Wang, J. Am. Chem. Soc. 126 (2004) 3422.
[40] X.W. Lou, C. Yuan, E. Rhoades, Q. Zhang, L.A. Archer, Adv. Funct. Mater. 16 (2006) 1679.
[41] X.C. Wang, J.C. Yu, Y.L. Chen, L. Wu, X.Z. Fu, Environ. Sci. Technol. 40 (2006) 2369.
[42] K.N.P. Kumar, J. Kumar, K. Keizer, J. Am. Ceram. Soc. 77 (1994) 1396.